# Spectroscopy and Dynamics of $Re^{4+}$ Near-IR-to-Visible Luminescence Upconversion

**Daniel R. Gamelin and Hans U. Güdel***

Department of Chemistry and Biochemistry, University of Bern, Freiestrasse 3, CH-3000 Bern 9, Switzerland

*Received May 19, 1999*

Intense visible upconversion luminescence is observed in a $Re^{4+}$-doped low-phonon host material, $Cs_2ZrCl_6$, with excitation in the near-infrared. The upconversion excitation wavelength, temperature, power, and time dependence is studied using variable-temperature absorption and luminescence spectroscopies, and modeled using a three-level set of coupled nonlinear rate equations. On the basis of analysis of these data, energy-transfer upconversion is shown to be the dominant mechanism responsible for this phenomenon. The main properties of this upconversion mechanism are correlated to properties of the $Re^{4+}$ electronic structure, in particular the large energy gaps, the small excited-state distortions, and the lack of cross-relaxation pathways for radiationless decay. These properties make this ion attractive for upconversion phosphor and laser materials applications, and two potential upconversion laser schemes are proposed. The contributions of these same properties to the photoredox chemistry of $Re^{4+}$ and related $d^3$ ions are discussed.

## I. Introduction

Materials displaying novel photophysical effects are currently receiving a tremendous amount of attention due to the anticipated roles such systems will play in future generations of photonic data communication, conversion, and storage devices. Among the photophysical processes considered promising in this regard is that of luminescence upconversion,[1,2] which is attractive both as a means of generating higher-energy photons from a low-energy photon source, and for the associated nonlinear optical properties of such upconversion materials. The vast majority of luminescence upconversion materials investigated to date have involved rare earth ions such as $Er^{3+}$ and $Nd^{3+}$.[1,2] Such ions are ideal from the perspective of having multiple luminescent excited states, and luminescence upconversion materials based on rare earth ions currently find use, for example, as solid-state lasers,[3] imaging phosphors,[4] and quantum counters in IR photon detection devices.[5] By contrast, relatively little attention has been given to the study of transition metals as upconversion ions, despite the advantages of increased oscillator strengths, broadband luminescence profiles, and synthetic flexibility potentially offered by transition metals relative to rare earth ions. Transition-metal luminescence upconversion has previously been reported for octahedral $Ti^{2+}$,[6] $Os^{4+}$,[7,8] and $Ni^{2+}$ [9,10] ions, representing the $d^2$, $d^4$, and $d^8$ electronic configurations, respectively, and very recently we communicated[11] the observation of low-temperature luminescence upconversion in $Re^{4+}$- and $Mo^{3+}$-doped halide lattices, constituting a preliminary report of the first upconversion observed in the $d^3$ class of transition metals. Already, this relatively small set of ions has revealed a rich variety of photophysical effects, including broadband upconversion luminescence,[6,9] two cases of photon avalanches,[8,10] and the recognition of important spin selection rule contributions that distinguish the transition-metal upconversion processes from those of the more commonly studied rare earth ions.[11] We are now involved in the systematic study of a variety of transition-metal doped low-phonon host materials with the objective of observing and describing new photophysical phenomena related to luminescence upconversion in these materials. As chemists, we are also fundamentally interested in the ability to control such processes by chemical tuning, and to achieve this goal a deep understanding of the physical processes behind these phenomena is required.

**Scheme 1**

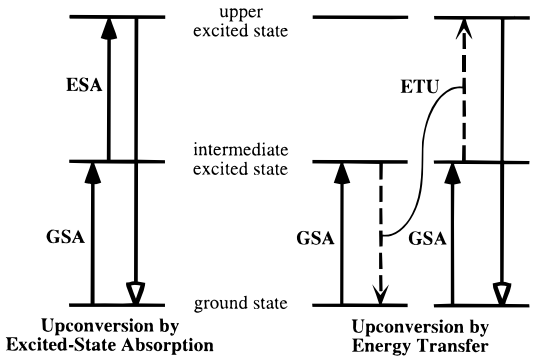


The basic prerequisite for luminescence upconversion in any material is the existence of two or more metastable excited states, as illustrated in Scheme 1. The first excited state serves

(1) Wright, J. C. In *Topics in Applied Physics: Radiationless Processes in Molecules and Condensed Phases*; Fong, F. K., Ed.; Springer: Berlin, 1976; pp 239−295.
(2) Auzel, F. E. *Proc. IEEE* **1973**, *61*, 758−786.
(3) Lenth, W.; Macfarlane, R. M. *Opt. Photon. News* **1992**, *3*, 8−15.
(4) Downing, E.; Hesselink, L.; Ralston, J.; Macfarlane, R. *Science* **1996**, *273*, 1185−1189.
(5) Chivian, J. S.; Case, W. E.; Eden, D. D. *Appl. Phys. Lett.* **1979**, *35*, 124−125.
(6) Jacobsen, S. M.; Güdel, H. U. *J. Lumin.* **1989**, *43*, 125−137.
(7) Wermuth, M.; Güdel, H. U. *Chem. Phys. Lett.* **1998**, *281*, 81−85.
(8) Wermuth, M.; Güdel, H. U. *J. Am. Chem. Soc*., in press.
(9) May, P. S.; Güdel, H. U. *J. Chem. Phys.* **1991**, *95*, 6343−6354.
(10) Oetliker, U.; Riley, M. J.; May, P. S.; Güdel, H. U. *Coord. Chem. Rev.* **1991**, *111*, 125−130 and references therein.
(11) Gamelin, D. R.; Güdel, H. U. *J. Am. Chem. Soc.* **1998**, *120*, 12143−12144.

10.1021/ic990556r CCC: $18.00 
Published on Web 10/12/1999

as an intermediate reservoir for the storage of one-photon excitation energy, while the upper state serves as the source for higher-energy luminescence. The two most common mechanisms for the conversion of intermediate excited ions into upper excited ions are those of excited-state absorption (ESA) and energy-transfer upconversion (ETU), illustrated in Scheme 1. In ESA, a singly-excited ion generated via ground-state absorption (GSA) is excited to the upper state through absorption of a second quantum of photon energy. ESA is therefore fundamentally a single-center process. In ETU, two singly-excited ions interact through a nonradiative energy-transfer process to generate one ion in the upper state and one in the ground state. This process is therefore fundamentally a multicenter phenomenon.

In this paper, we present a detailed report of the luminescence upconversion in $Re^{4+}$:$Cs_2ZrCl_6$. Much effort has already been given to describing the electronic structure of this ion based on the high-resolution study of its absorption and luminescence spectra.[12−19] $Re^{4+}$ and its isoelectronic analogs $Mo^{3+}$ and $W^{3+}$ have also been recognized as attractive starting materials for multielectron photoredox chemistry due to their long-lived excited states and to the accessibility of a series of higher oxidation states in these ions.[20−23] Here, variable-temperature CW and dynamic absorption and luminescence spectroscopic techniques are used to determine the upconversion mechanism active in $Re^{4+}$:$Cs_2ZrCl_6$. A wide variety of thermal and temporal spectroscopic data are simulated using an experimentally-parametrized kinetic model, and analysis of these parameters shows that the remarkable upconversion efficiency displayed by this ion is attributable to properties inherent to its electronic structure. On the basis of these results, two viable schemes for upconversion lasing action are proposed. Finally, the role of the $Re^{4+}$ electronic structure in its photoredox chemistry is discussed.

## II. Experimental Section

$Re^{4+}$-doped $Cs_2ZrCl_6$ samples were synthesized at ca. 820 °C from stoichiometric admixtures of CsCl, $ZrCl_4$, and $Cs_2ReCl_6$, and single crystals were grown from the melts by the Bridgeman technique. All samples and precursors were handled under inert nitrogen and helium atmospheres only. For both absorption and luminescence studies, monolithic samples were sealed from the atmosphere under a partial pressure of He, which serves as a heat transmitter. Absorption spectra were collected on a Cary 5e spectrometer using closed-cycle cryogenic cooling (Air Products). Sample concentrations were determined on the basis of published solution $\epsilon$ values at 300 K.[21]

Downconversion luminescence spectra were excited with a He:Ne laser, a $Kr^+$ laser, or a Nd:$LiYF_4$ laser (*vide infra*). Sample luminescence was dispersed through a 3/4 m single monochromator (Spex 1702) or a 0.85 m double monochromator (Spex 1402), and detected by a PMT (RCA C31034 or Hamamatsu 3310-01, Stanford Research 430 photon counting) or a Ge photodiode (ADC403L, Stanford Research 830 lock-in amplification). $Re^{4+}$ excitation spectra were excited with a 100 W halogen lamp dispersed through a 3/4 m single monochromator (Spex 1702), and the broadband upconversion luminescence was detected by a PMT (RCA C31034). Typical powers in $Re^{4+}$ excitation scans were ca. 4 $\mu$W/mm$^2$. Sample cooling was achieved using a quartz He flow tube. Lifetime measurements used pulsed excitation from a Nd:YAG (Quanta Ray DCR 3, 20 Hz, 1064 nm) or generated by an acoustooptic modulator (Coherent 305, Stanford Research DS 345 function generator). Signals were detected with the same photomultipliers and recorded using a multichannel scaler (Stanford Research 430) or with a fast Ge detector (ADC403HS, 1 $\mu$s response) and recorded using an oscilloscope (Tektronix TDS 540A).

Excitation in the power dependence measurements and room-temperature near-IR luminescence scans was obtained from a home-built Nd:$LiYF_4$ laser (1047 nm), pumped by an $Ar^+$ (Spectra Physics 2060-10 SA) pumped Ti:sapphire laser (Spectra Physics 3900 S) using a neutral density filter wheel to attenuate the pump power. Luminescence signals were passed through a 0.27 m monochromator (Spex 270M) and detected by a Si/GaInAs detector (Spex DSS-SIGA020A, Stanford Research 510 lock-in amplifier).

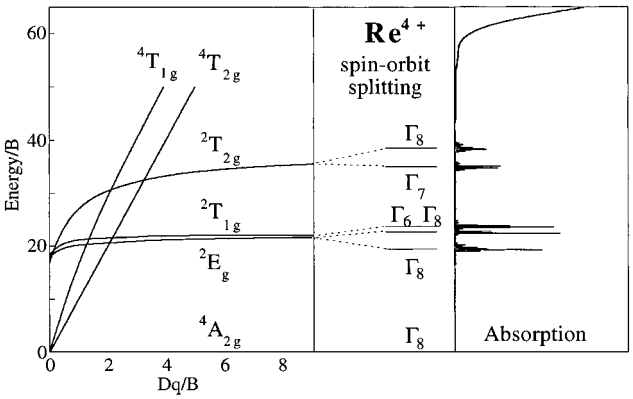


**Figure 1.** Tanabe−Sugano energy level diagram showing the first few excited states of the $d^3$ configuration, the spin−orbit splitting of the doublets, and the experimental 10 K overview absorption spectrum of $Re^{4+}$:$Cs_2ZrCl_6$.

## III. Results and Analysis

**A. Absorption and CW Downconversion Luminescence.** Several detailed reports of the low-temperature $Re^{4+}$ absorption and luminescence spectra have been previously published.[12−18] Only the key properties of these spectra will be summarized here, and new observations related to the photophysics of this ion will instead be emphasized. Figure 1 shows an overview 10 K absorption spectrum of 2.5% $Re^{4+}$:$Cs_2ZrCl_6$, and correlates the lowest-energy absorption features to the appropriate region of a $d^3$ Tanabe−Sugano energy-level diagram. This absorption spectrum shows a series of excited-state multiplets derived from formally spin-flip ligand-field-independent electronic transitions. The energies of these transitions in $Re^{4+}$ ions are determined by interelectron repulsion, and may vary due to the nephelauxetic effect: In complexes involving greater M−L covalency, these transitions are all shifted to lower energy (e.g., by an average of 320 cm$^{-1}$ (3%) in $ReBr_6^{2-}$ [16,19]), while in those involving less covalency they occur at higher energy (e.g., by an average of 2400 cm$^{-1}$ (22%) in $ReF_6^{2-}$ [17]). To higher energy, a broad, intense absorption beginning at ca. 27 000 cm$^{-1}$ marks the onset of the $Cl^- \rightarrow Re^{4+}$ LMCT transitions.[13] Figure 2 shows the spin-flip region of this absorption spectrum in greater detail, at low and high temperatures. The octahedral site symmetry and the ligand-field independence of these excited states result

(12) Dorain, P. B.; Wheeler, R. G. *J. Chem. Phys.* **1966**, *45*, 1172−1181.
(13) Collingwood, J. C.; Piepho, S. B.; Schwartz, R. W.; Dobosh, P. A.; Dickenson, J. R.; Schatz, P. N. *Mol. Phys.* **1975**, *29*, 793−814.
(14) Yoo, R. K.; Lee, S. C.; Kozikowski, B. A.; Keiderling, T. A. *Chem. Phys.* **1987**, *117*, 237−254.
(15) Black, A. M.; Flint, C. D. *J. Chem. Soc., Farraday Trans. 2* **1977**, *73*, 877−885.
(16) Flint, C. D.; Paulusz, A. G. *Chem. Phys. Lett.* **1979**, *62*, 259−260.
(17) Black, A. M.; Flint, C. D. *J. Mol. Spec.* **1978**, *70*, 481−483.
(18) Flint, C. D.; Paulusz, A. G. *Mol. Phys.* **1981**, *43*, 321−334.
(19) Black, A. M.; Flint, C. D. *J. Chem. Soc., Faraday Trans. 2* **1975**, *71*, 1871−1876.
(20) Yao, Q.; Maverick, A. W. *J. Am. Chem. Soc.* **1986**, *108*, 5364−5365.
(21) Maverick, A. W.; Lord, M. D.; Yao, Q.; Henderson, L. J., Jr. *Inorg. Chem.* **1991**, *30*, 553−558.
(22) Mohammed, A. K.; Isovitsch, R. A.; Maverick, A. W. *Inorg. Chem.* **1998**, *37*, 2779−2785.
(23) Yao, Q.; Maverick, A. W. *Inorg. Chem.* **1988**, *27*, 1669−1670.

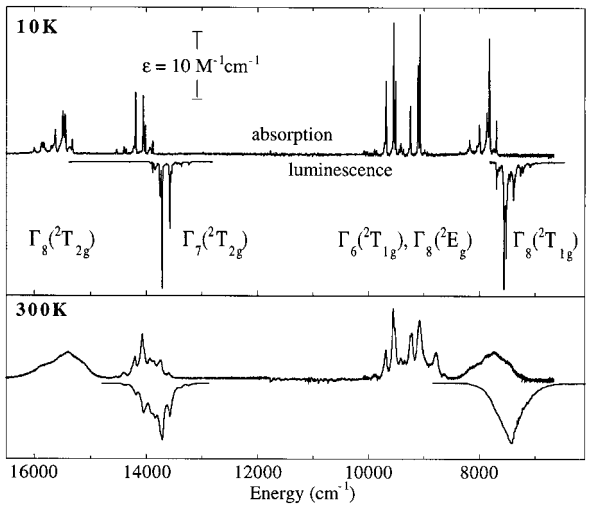


**Figure 2.** Absorption and luminescence spectra (10 and 300 K) of 2.5% $Re^{4+}$:$Cs_2ZrCl_6$. Luminescence intensities are with direct excitation into absorption features of the same energy region, and have been separately normalized.

in the dominance of vibronic origins and the lack of significant overtone intensities, reflecting undistorted nuclear geometries in all of these excited states. Substantial absorption intensity and bandshape changes are observed as the sample is warmed from 10 to 300 K.

Figure 3a shows the temperature dependence of the integrated absorption intensities for the four multiplets shown in Figure 2. These data reveal that all intensities increase with increasing temperature, and that the temperature dependence is the same for each multiplet. The total integrated intensities of these absorption features are approximately 3 times larger at room temperature than at 10 K. The dashed lines in Figure 3a show the best fits of these data by eq 1,[24] which describes this

$$\frac{I(T)}{I(T_0)} = \coth\left(\frac{\nu_{\text{eff}}}{2kT}\right) \tag{1}$$

temperature dependence as resulting from thermal population of ungerade excited vibrational levels of the ground electronic state upon warming, leading to hot-band absorption intensity. These fits yield a value of $\nu_{\text{eff}} = 143 \pm 15$ cm$^{-1}$ for the effective energy of the ungerade activating mode. This value is between those of the first two intense vibronic origins, $\nu_6 = 138$ cm$^{-1}$ and $\nu_4 = 174$ cm$^{-1}$, observed in low-temperature luminescence spectra, respectively, and reflects thermal excitation of both of these ungerade ground-state vibrations. As shown in Figure 2, luminescence is also observed from both the lower, $^2T_{1g}/^2E_g$, and upper, $^2T_{2g}$, excited-state multiplets, at both low and high temperatures. The vibronic structure of these luminescence transitions is analogous to that of the corresponding absorption processes, and both luminescent transitions show substantial vibronic hot-band intensity at elevated temperatures.

The observation of two well-separated luminescent excited states in $Re^{4+}$ is remarkable in that it represents a rare transition-metal exception to Kasha's rule,[25] which recognizes that luminescence generally derives only from one excited state of a given spin multiplicity, typically the lowest. This generalization arises because nonradiative relaxation of upper excited states

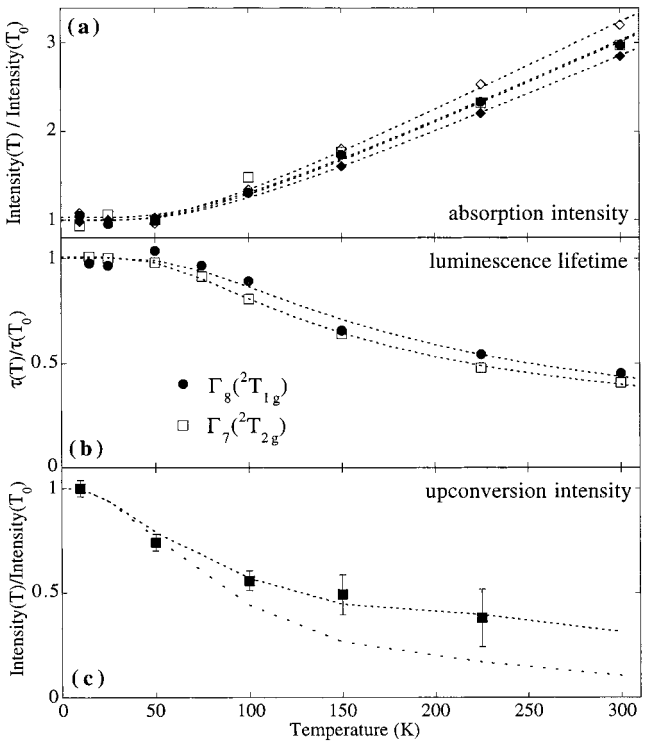


**Figure 3.** Temperature dependence of (a) integrated absorption intensities, (b) luminescence lifetimes, and (c) double-integrated upconversion intensities in 2.5% $Re^{4+}$:$Cs_2ZrCl_6$ (integrated monochromatic excitation scans with broadband detection). The experimental data points correspond to the following excited states: (●) $\Gamma_8(^2T_{1g})$, (◆) $\Gamma_8(^2T_{2g})$, (◇) $\Gamma_8(^2E_g)/\Gamma_6(^2T_{1g})$, (□) $\Gamma_7(^2T_{2g})$, (■) average($^2T_{1g}/^2E_g$). Error bars in (c) are estimated from differences between $\Gamma_8(^2T_{1g})$ and $\Gamma_8(^2E_g)/\Gamma_6(^2T_{1g})$ measurements. Fits (- - -) of the absorption ($\nu_{\text{eff}} = 143 \pm 15$ cm$^{-1}$) and lifetime ($\nu_{\text{eff}} = 160 \pm 20$ cm$^{-1}$) data using eq 1 are also shown. Calculated upconversion temperature dependencies are included in (c), neglecting (- - -) and including (----) a $w_{\text{ETU}}$ temperature dependence as described in section III.C.iii.

to the lowest excited state is often extremely rapid. The total decay rate constant, $k_{\text{decay}}$, of any excited state is the sum of all radiative (rad) and nonradiative (nr) decay contributions, and defines the observed lifetime of that state, $\tau_{\text{obsd}}$, as described by eq 2. In the absence of cross-relaxation mechanisms, $k_{\text{nr}}$ is

$$k_{\text{decay}} = k_{\text{rad}} + k_{\text{nr}} = \tau_{\text{obsd}}^{-1} \tag{2}$$

dominated by multiphonon relaxation processes, $k_{\text{mp}}$, in which excitation energy is transformed to heat by excitation of lattice phonons. In cases where excited-state nuclear distortions are small, the weak-coupling energy-gap law of eq 3 is found to

$$k_{\text{mp}}(0) \approx \beta \exp[-p \ln(p/S) + p] \tag{3}$$

effectively describe the $T = 0$ K multiphonon decay rate constant.[26,27] Here, $p = \Delta E_{0-0}/\nu_{\text{max}}$ is the energy gap between the luminescent state and the closest lower-energy state in units of the largest vibrational quantum energy, $\nu_{\text{max}}$ (cm$^{-1}$), the prefactor $\beta$ contains the electronic part of the transition matrix element, and $S$ is the Huang−Rhys dimensionless excited-state distortion parameter in units of vibrational quanta of the distorting nuclear coordinate. Equation 3 shows a strong inverse

(24) Ballhausen, C. J. *Introduction to Ligand Field Theory*; McGraw Hill: New York, 1962.
(25) Kasha, M. *Discuss. Faraday Soc.* **1950**, *9*, 14−19.
(26) Englman, R.; Jortner, J. *J. Mol. Phys.* **1970**, *18*, 145−164.
(27) van Dijk, J. M. F.; Schuurmans, M. F. H. *J. Chem. Phys.* **1983**, *78*, 5317−5323.

dependence of $k_{mp}$ on $p$. Additionally, for a given energy gap $p$, the introduction of even small excited-state distortions, $S$, can rapidly enhance radiationless multiphonon relaxation rates.

The reduced energy gaps in $ReCl_6^{2-}$, determined from Figure 2, are $p_1 \approx 22$ and $p_2 \approx 12$ ($\nu_{max} = \nu_1(a_{1g}) = 342$ cm$^{-1}$). The excited-state distortion magnitudes are determined from overtone intensities in the $\nu_1(a_{1g})$ core expansion mode to be $S_1(\Gamma_8(^2T_{1g})) = 0.20$ and $S_2(\Gamma_7(^2T_{2g})) = 0.11$. These excited-state distortions are 2 orders of magnitude smaller than the corresponding $p$ values. $ReCl_6^{2-}$ therefore resembles rare earth ions, which generally show small excited-state distortions, and for which values of $p \geq 6$ are typically observed to lead to negligible radiationless relaxation rates. Although the threshold value for $p$ may be somewhat larger in transition metals than in rare earth ions due to greater electron−phonon coupling strengths and vibrational anharmonicities, the $ReCl_6^{2-}$ energy gaps are large enough that intense luminescence is observed from the electronic states immediately above both gaps. The large energy gaps, low phonon energies, and small excited-state distortions reflected in the absorption and luminescence spectra of Figure 2 are therefore essential to the existence of substantial upper-excited-state lifetimes in this ion.

Significantly, emission is observed only from the lowest energy spinor component of each excited-state multiplet in this host lattice. The largest energy gaps between the components of each multiplet are $p = 3.7$ in $^2T_{1g}/^2E_g$ and $p = 4.3$ in $^2T_{2g}$, and these are evidently too small to prevent rapid relaxation to the lowest component.[28] The multitude of electronic and vibronic transitions observed in the absorption spectrum (Figure 2) thus serve the function of harvesting excitation energy and feeding it to the lowest state of the multiplet, and the energy level diagram of $Re^{4+}$ is therefore effectively analogous to the three-level systems shown in Scheme 1. The observation of luminescence from two different excited states satisfies the basic prerequisite of luminescence upconversion suggested by this scheme. Moreover, as seen in Figure 2, the energy of the intermediate state ($\Gamma_8(^2T_{1g})$, 7695 cm$^{-1}$ origin) is very nearly half that of the upper excited state ($\Gamma_8(^2T_{2g})$, 13885 cm$^{-1}$ origin), indicating that good energetic conditions may exist for one or both of the two-photon upconversion processes presented in Scheme 1.

**B. Downconversion Luminescence Dynamics.** Parts a and b of Figure 4 show the luminescence decay dynamics of the $\Gamma_8(^2T_{1g})$ and $\Gamma_7(^2T_{2g})$ excited states at two temperatures, following direct low-power laser excitation into each state. Under these conditions, the excited-state populations decay monoexponentially, and are seen to decay on a shorter time scale at 300 K ($\tau_{near-IR} = \tau_1 = 909$ $\mu$s, $\tau_{vis} = \tau_2 = 48$ $\mu$s) than at 10 K ($\tau_1 = 1981$ $\mu$s, $\tau_2 = 118$ $\mu$s). Lifetime data measured between 10 and 300 K are plotted in Figure 3b, from which it is observed that the lifetimes of both luminescent excited states decrease by ca. 60% between 10 and 300 K. Since the two luminescence processes show nearly identical temperature dependence despite the fact that their energy gaps differ by ca. 50% (22 vs 12 quanta of $\nu_{max}$), we reach the important conclusion that the observed lifetimes of both excited states are entirely radiative even at room temperature. This conclusion is quantitatively supported by the observation that the $\Gamma_8(^2T_{1g})$ lifetime data of Figure 3b can be accurately predicted from this

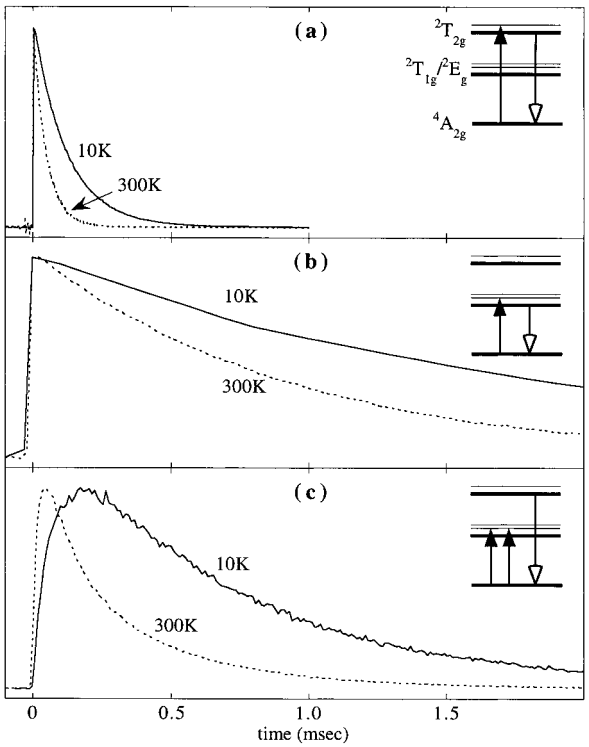


**Figure 4.** Luminescence dynamics of 2.5% $Re^{4+}$:$Cs_2ZrCl_6$ at 10 (—) and 300 K (----) for (a) the visible (632.8 nm excitation) and (b) near-IR (1064 nm excitation) downconversion processes, and for (c) the visible upconversion process following a 10 ns (1064 nm) laser pulse. The respective excitation and emission processes are indicated schematically.

state's absorption intensity by assuming purely radiative decay processes: As shown in eq 4,[29] the radiative decay rate constant

$$k_{rad} = f\frac{g_{gr}}{g_{ex}}\frac{n[(n^2+2)/3]^2}{\alpha\lambda^2} \qquad (4)$$

of eq 2 is directly proportional to the oscillator strength, $f$, of the corresponding absorption transition. Here, $\alpha$ is a constant equal to $1.5 \times 10^4$ s/m$^2$, $g$ is the degeneracy of the indicated state, $\lambda$(m) is the wavelength of the relevant electronic transition, and $n$ is the polarization-averaged index of refraction at this wavelength. Using eq 4 and the measured 10 K oscillator strength of $f = 4.0 \times 10^{-6}$ for the lowest-energy $\Gamma_8(^4A_{2g}) \leftrightarrow \Gamma_8(^2T_{1g})$ electronic transition in Figure 2 yields a calculated[30] $k_{rad,1}(10\text{ K}) = 476$ s$^{-1}$, or a predicted radiative lifetime of $\tau_1(10\text{ K})_{calcd} = 2.1$ ms, in good agreement with the observed 10 K lifetime of $\tau_1(10\text{ K}) = 2.0$ ms. The increase in integrated absorption intensity by a factor of 3 observed in Figure 3a leads to a corresponding three-fold increase to $k_{rad,1}(300\text{ K})_{calcd} = 1428$ s$^{-1}$, or $\tau_1(300\text{ K})_{calcd} = 0.7$ ms, consistent with the observed value of $\tau_1(300\text{ K}) = 0.9$ ms. Additionally, fits of the variable-temperature lifetime data to the inverse of eq 1 yield $\nu_{eff} = 160 \pm 20$ cm$^{-1}$ for the vibronic levels affecting visible and near-IR luminescence lifetimes, in agreement with the value obtained in Figure 3a ($\nu_{eff} = 143 \pm 15$ cm$^{-1}$)[31] and the lowest ungerade

(28) Independent low-temperature $\Gamma_8(^2T_{2g})$ luminescence has been observed in $Re^{4+}$:$Cs_2ZrBr_6$, where $p \approx 8.9$ (refs 16 and 19).

(29) Imbusch, G. F. In *Luminescence Spectroscopy*; Lumb, M. D., Ed.; Academic: New York, 1978; pp 1−92.

(30) The following values were used: $f = 4.0 \times 10^{-6}$, $\lambda = 1.299 \times 10^{-6}$ m, $n = 1.5$, $g_{gr} = 4$, $g_{ex} = 4$.

(31) Note that erroneous application of this model to a system involving significant nonradiative decay at high temperature would lead to $\nu_{eff}$ values smaller than those obtained from the corresponding absorption data.

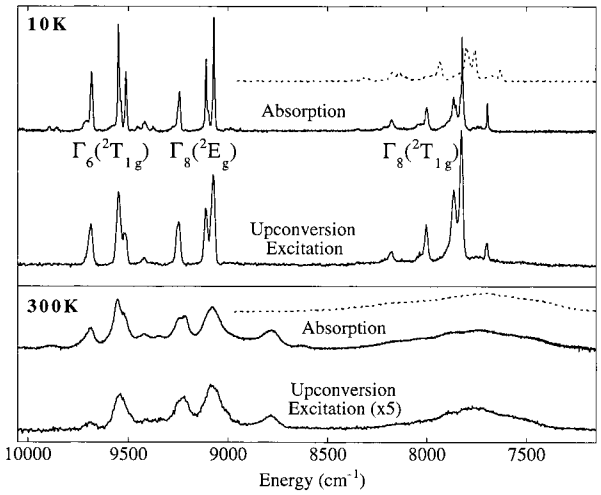


**Figure 5.** Absorption and upconversion excitation spectra (10 and 300 K) of 2.5% $Re^{4+}$:$Cs_2ZrCl_6$ in the $^2T_{1g}/^2E_g$ region. The dashed line is the estimated $\Gamma_8(^2T_{1g}) \rightarrow {}^2T_{2g}$ ESA spectrum obtained by subtraction of the $\Gamma_8(^2T_{1g})$ origin energy (7695 $cm^{-1}$) from the GSA spectrum. Upconversion excitation spectra were obtained with broadband detection of the $\Gamma_7(^2T_{2g}) \rightarrow \Gamma_8(^4A_{2g})$ upconverted luminescence.

vibrational energies observed in the absorption spectra of these states. Although the similar temperature dependence of the upper excited-state ($\Gamma_7(^2T_{2g})$) lifetime in Figure 3b also confirms its radiative origin, the value of $k_{rad,2}(10\ K) = 2137\ s^{-1}$ ($\tau_{rad,2}(10\ K) = 0.47$ ms) calculated from its GSA intensity is 4 times smaller than the observed $k_{decay,2}(10\ K) = 8432\ s^{-1}$ ($\tau_2(10\ K) = 0.12$ ms), indicating contributions from additional inter-excited-state radiative processes (*vide infra*). In summary, this analysis demonstrates that the observed lifetimes for both luminescent excited states are purely radiative, even at room temperature, and the principal cause for the reduced lifetimes of both luminescent excited states at elevated temperatures is the increase in oscillator strengths, *f*, and hence in *radiative* decay rates, $k_{rad}$.

**C. Upconversion Luminescence. i. Upconversion Excitation Wavelength Dependence and Kinetic Model.** As communicated recently,[11] near-IR excitation of $Re^{4+}$ in $Cs_2ZrCl_6$ leads to visible upconversion luminescence. Figure 5 shows low- and high-temperature excitation scans of this upconversion luminescence, in which the total $^2T_{2g}$ luminescence is monitored as a function of monochromatic excitation energy in the $^2T_{1g}/^2E_g$ energy region. Upconversion excitation scans closely follow the near-IR absorption spectra from 10 to 300 K, and no additional features are observed at any temperature or wavelength. These excitation scans can be divided into two distinct regions: the lower-energy $\Gamma_8(^2T_{1g})$ excited state and the higher-energy $\Gamma_6(^2T_{1g})$ and $\Gamma_8(^2E_g)$ excited states. Also shown in Figure 5 is the estimated $\Gamma_8(^2T_{1g})$ ESA spectrum obtained by shifting the GSA spectrum by the energy of the $\Gamma_8(^2T_{1g})$ electronic origin (7695 $cm^{-1}$), justified by the fact that the intermediate excited state has the same electronic configuration and geometry as the ground state. From Figure 5 it is seen that in the lower energy region the photon energies may be simultaneously in resonance with both $\Gamma_8(^4A_{2g}) \rightarrow \Gamma_8(^2T_{1g})$ GSA excitation and $\Gamma_8(^2T_{1g}) \rightarrow \Gamma_8(^2T_{2g})$ ESA excitation. Contributions from a GSA/ESA upconversion mechanism are therefore possible in this energy range. By contrast, photons energetic enough to excite the higher energy $\Gamma_8(^4A_{2g}) \rightarrow \Gamma_6(^2T_{1g})$ and $\Gamma_8(^2E_g)$ GSA transitions are too energetic to lead to ESA, and GSA/ESA upconversion in this region of the excitation scan is therefore not possible. The absence of new spectral features in both regions of the excitation spectra rules out significant GSA/ESA contributions to the upconversion luminescence intensities and indicates a dominant GSA/ETU mechanism. This, combined with the conclusion of an effective three-level description of the $Re^{4+}$ electronic structure (section III.A), allows the use of Scheme 2 to model the observed photophysics.

**Scheme 2**

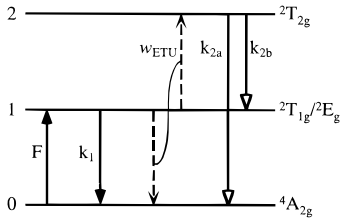


The dynamics associated with Scheme 2 can be described by the coupled nonlinear rate equations presented in eq 5, where

$$\begin{aligned} dN_0/dt &= -FN_0 + k_1N_1 + k_{2a}N_2 + w_{ETU}(N_1)^2 \\ dN_1/dt &= FN_0 - k_1N_1 + k_{2b}N_2 - 2w_{ETU}(N_1)^2 \\ dN_2/dt &= -(k_{2a} + k_{2b})N_2 + w_{ETU}(N_1)^2 \end{aligned} \qquad (5)$$

*F* is the ground-state absorption rate constant and $N_0$, $N_1$, and $N_2$ correspond to the population densities (ions/$cm^3$) of the $^4A_{2g}$, $^2T_{1g}/^2E_g$, and $^2T_{2g}$ electronic levels, respectively. $w_{ETU}$ ($cm^3\ s^{-1}$) is the effective rate parameter governing energy-transfer upconversion. Equation 5 assumes that all ions are effectively equivalent, and hence that the behavior of the ensemble of dopant ions can be described by average kinetic parameters. As described above, $k_1$ and $k_{2a} + k_{2b}$ are obtained experimentally by measuring $\tau_1$ and $\tau_2$. To deconvolute $k_{2a}$ and $k_{2b}$, we take advantage of the fact that only radiative processes contribute to the observed luminescence decay rates. With this knowledge, $k_{2a}$ is directly determined from eq 4 and the oscillator strength of the $\Gamma_8(^4A_{2g}) \rightarrow \Gamma_7(^2T_{2g})$ GSA transition. The difference between $k_{2a}$ and the observed $k_{2a} + k_{2b} = \tau_2^{-1}$ then provides $k_{2b}$. This yields values of $k_{2a} = 2137\ s^{-1}$ and $k_{2b} = 6295\ s^{-1}$ at 10 K. Since $k_{2a}$ and the sum $k_{2a} + k_{2b} = \tau_2^{-1}$ both increase by factors of ca. 3 upon warming to 300 K (*vide supra*), $k_{2b}$ must also have a similar temperature dependence (*i.e.*, the ratio $k_{2b}/k_{2a}$ is essentially temperature independent). The ETU rate parameter $w_{ETU}$ is determined experimentally from the short time region of the near-IR luminescence decay transients under high-power conditions (see the Appendix).[32] This analysis yields a value of $w_{ETU} = 5.8 \times 10^{-16}\ cm^3\ s^{-1}$ at 300 K, or $1.9 \times 10^{-16}\ cm^3\ s^{-1}$ at 10 K, with estimated error bars of ca. 50%. These experimentally determined kinetic parameters for the processes depicted in Scheme 2 are summarized in Table 1.

The parameters presented in Table 1 reveal an important aspect of this upconversion mechanism, namely, that the rate constant for inter-excited-state luminescence, $k_{2b}$, is significantly larger than the rate constants for transitions to the ground state, $k_1$ and $k_{2a}$. This is attributable to two factors: First, the inter-excited-state transitions are spin-allowed $^2\Gamma \rightarrow {}^2\Gamma$ transitions, whereas those involving the ground state are spin-forbidden $^2\Gamma \rightarrow {}^4\Gamma$ transitions (see Scheme 2). This factor is moderated by the large spin−orbit coupling active in $Re^{4+}$, but nevertheless leads to greater inter-excited-state oscillator strengths. Second, with a ground-state degeneracy of $g_0(^4A_{2g}) = 4$, and excited-

(32) Jensen, T. Ph.D. Thesis, Institute of Laser Physics, University of Hamburg, 1996.

**Table 1.** Kinetic Parameters Used in Eq 5 Determined for 2.5% $Re^{4+}$:$Cs_2ZrCl_6$

| transition | label (Scheme 2, eq 5) | rate constant ($s^{-1}$) 10 K | rate constant ($s^{-1}$) 300 K | $\nu_{av}$ ($cm^{-1}$) |
|---|---|---|---|---|
| $\Gamma_8(^2T_{1g}) \rightarrow \Gamma_8(^4A_{2g})$ | $k_1$ | 505 | 1101 | 7400 |
| $\Gamma_7(^2T_{2g}) \rightarrow \Gamma_8(^4A_{2g})$ | $k_{2a}$ | 2137 | 5243 | 13600 |
| $\Gamma_7(^2T_{2g}) \rightarrow {}^2T_{1g}/{}^2E_g$ | $k_{2b}$ | 6295 | 15475 | (6200, 4800) |
| power-independent ETU Parameter | $w_{ETU}$ ($cm^3$) | $1.9 \times 10^{-16}$ | $5.8 \times 10^{-16}$ | |
| ETU rate constant at ca. 75 $mW/mm^2$ (1047 nm) | $2w_{ETU}N_1$ | | 4630 | |

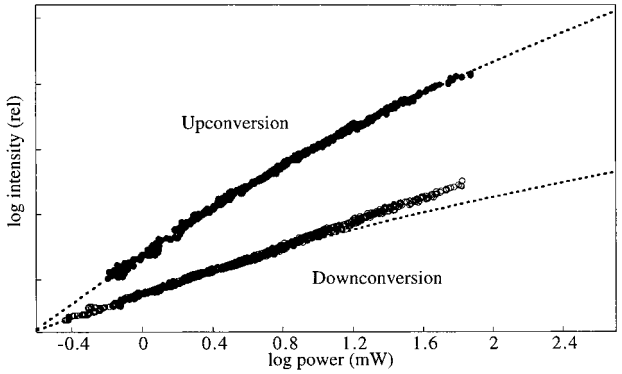


**Figure 6.** Pump-power dependence of the upconversion and downconversion luminescence intensities in 2.5% $Re^{4+}$:$Cs_2ZrCl_6$ at 300 K. Excitation is at 9551 $cm^{-1}$ (1047 nm) into $\Gamma_6(^2T_{1g})$. The dashed lines were calculated from eq 5 and the parameters in Table 1.

state degeneracies of $g_1(^2T_{1g}/^2E_g) = 10$ and $g_2(^2T_{2g}) = 6$, the large disparity in state multiplicities weights Scheme 2 in favor of inter-excited-state transitions, as described by eq 4 (or an analogous equation for inter-excited-state processes). Together, the spin selection rule and degeneracy weighting provide a significant bias to inter-excited-state transition rates, leading to an overall upper-excited-state decay ratio of $k_{2b}/k_{2a} \approx 3$, and allowing these rates to be competitive with those to the ground state despite the significant difference in the $\lambda^2$ contribution to these rate constants (eq 4). Similarly, the favorable oscillator strengths and degeneracies contribute to energy-transfer upconversion due to the dependence of nonradiative energy-transfer rate constants on oscillator strengths (*vide infra*). These important factors thus contribute to the upconversion performance of this ion by capturing excitation energy in the cycle of excited states through enhancement of both ETU and inter-excited-state luminescence transitions relative to radiative relaxation to the ground state. In the following sections, this kinetic model will be used to describe the power, temperature, and time dependence of the upconversion luminescence in $Re^{4+}$:$Cs_2ZrCl_6$.

**ii. Upconversion Power Dependence.** Figure 6 plots the visible upconversion and near-IR downconversion luminescence intensities versus 9551 $cm^{-1}$ (1047 nm) CW excitation powers on a double-log scale. At low powers, the slope of this upconversion power dependence is 2.0,[11] indicating that the $Re^{4+}$ upconversion luminescence intensity follows the quadratic behavior anticipated for a two-photon process. At higher excitation powers, however, deviation from this quadratic power dependence is observed as the slope decreases substantially, reaching a value of only 1.1 at the highest experimental power. Thus, at high excitation powers, this system shows a nearly linear power dependence for what is formally a two-photon excitation process. The near-IR luminescence power dependence is almost constant in this same power range, diminishing from a slope of 1.0 to a slope of 0.9 at high excitation powers in Figure 6.

This remarkable behavior can be understood by evaluation of the role of the pump excitation rate, $FN_0$, in the kinetic model described by eq 5. Quantitatively, the power dependence can be simulated using the full eq 5 and the parameters in Table 1 by solving explicitly for the steady-state (CW excitation) populations $N_1$ and $N_2$ at various pump rates, $FN_0$. The calculated curves are included in Figure 6. Each shows a linear asymptotic behavior at both low and high powers. Under steady-state conditions, these two limiting regimes can be identified with the relative magnitudes of the two competitive depletion mechanisms affecting the intermediate level population, $N_1$, namely, those of downconversion luminescence (rate constant $k_1$) and ETU (rate constant $2w_{ETU}N_1$). In the low-power limit, the excitation density, $N_1$, is very small, and $k_1 \gg 2w_{ETU}N_1$. In this limit, the intermediate level population behaves essentially as it would in the absence of upconversion, and the ions that participate in upconversion represent only a small perturbation. The $N_1$ and $N_2$ power dependencies obtained from the steady-state solution of eq 5 in this limit are given in eqs 6a and 6b, respectively.[33] In the high-power limit the excitation density

low-power limit:

$$N_1 \approx \frac{1}{k_1}(FN_0) \tag{6a}$$

$$N_2 \approx \frac{w_{ETU}}{k_1^2(k_{2a} + k_{2b})}(FN_0)^2 \tag{6b}$$

$N_1$ is very large, and $2w_{ETU}N_1 \gg k_1$. In this limit, ETU is the principal mechanism for depletion of the intermediate-level population. Solving eq 5 in this limit yields different expressions for the power dependence of the two excited-state populations, as shown in eqs 6c and 6d.[33,34] The upconversion luminescence

high-power limit:

$$N_1 \approx \left[\frac{(k_{2a} + k_{2b})}{w_{ETU}(2k_{2a} + k_{2b})}(FN_0)\right]^{1/2} \tag{6c}$$

$$N_2 \approx \frac{1}{2k_{2a} + k_{2b}}(FN_0) \tag{6d}$$

intensity, which is proportional to $N_2$, is therefore predicted to follow a quadratic dependence on pump rate in the low-power limit, but to reduce to a linear dependence on pump rate in the high-power limit. Similarly, the near-IR luminescence intensity, which is proportional to $N_1$, is predicted to be linearly dependent upon pump power in the low-power limit, and should show a square-root power dependence when the high-power limit is reached. The intermediate regions of slope ≈1.5 (upconversion)

(33) Pollnau, M.; Gamelin, D. R.; Lüthi, S. R.; Güdel, H. U.; Hehlen, M. P., submitted for publication.
(34) At extremely high pumping rates, ground-state population depletion may become significant, and deviation from the high-power behavior of eqs 6c and 6d will occur.

and slope ≈0.75 (downconversion) correspond to powers at which $2w_{ETU}N_1$ and $k_1$ are competitive in magnitude.

From this analysis, the luminescence power dependence shown in Figure 6 can be rationalized. The experimental change from 2.0 to 1.1 observed in the upconversion power dependence is described both qualitatively and quantitatively by eqs 5 and 6 as corresponding to a shift from the low- to the high-power limit. From the power dependence simulations, a value of $2w_{ETU}N_1 \approx 4.2k_1$ is estimated at the highest experimental power used (ca. 75 mW/mm$^2$), which corresponds to an intermediate-level branching ratio of $\eta_{ETU} = 0.4$, where $\eta_{ETU}$ is defined as in eq 7. Note that the maximum branching ratio is $\eta_{ETU} = 0.5$

$$\eta_{ETU} = \frac{w_{ETU}N_1}{2w_{ETU}N_1 + k_1} \tag{7}$$

due to the two-ion nature of the ETU process (Scheme 1). With a pump power of ca. 75 mW/mm$^2$ we are thus close to this theoretical maximum in 2.5% Re:$Cs_2ZrCl_6$. In contrast with the upconversion power dependence, only a small reduction in slope is observed between low and high powers in the near-IR downconversion power dependence shown in Figure 6, indicating that a significant number of ions are found only in the ground or first excited states. This behavior is attributed to the presence of inhomogeneous $Re^{4+}$ excitation densities under real experimental conditions. Microscopically, this may derive from photophysical differences between spatially-isolated vs clustered dopant ions, or between low- vs high-photon-density regions in the real three-dimensional sample. Both scenarios would result in a range of microscopic upconversion rates, since both involve a range of microscopic excitation densities. Such a range in microscopic upconversion rates would lead to the observation of different populations contributing to upconversion and downconversion luminescence signals under the high-power excitation conditions of Figure 6. Both scenarios also imply finite energy migration within the crystal.[1] This general conclusion is confirmed by simultaneous analysis of the upconversion and downconversion luminescence dynamics (*vide infra*).[35]

The high-power 300 K near-IR luminescence spectra observed with near-IR excitation (9551 cm$^{-1}$ (1047 nm), CW) shown in Figure 7 also probe the intermediate-level branching ratios under steady-state conditions. As indicated in Figure 7, the near-IR luminescence spectra in the region between 5500 and 8500 cm$^{-1}$ have both $^2T_{1g} \rightarrow {}^4A_{2g}$ and $^2T_{2g} \rightarrow {}^2T_{1g}/{}^2E_g$ luminescence contributions. The relative intensities of these two luminescences reflect the steady-state branching ratio of the intermediate level. This is illustrated by comparison of the data obtained with 2.5% and 5% dopant concentrations. The 2-fold increase in inter-excited-state intensity relative to downconversion intensity on increasing the $Re^{4+}$ concentration from 2.5% to 5% indicates that this branching ratio is approximately twice as large in the more concentrated sample. This increase reflects both the increased excitation density, $N_1$, due to the higher optical density of the higher concentration sample, as well as an increased $w_{ETU}$, which depends heavily on interionic distances (*vide infra*) and hence is enhanced by higher doping levels. Both of these factors contribute to increasing the upconversion rate constant $2w_{ETU}N_1$ relative to $k_1$, thereby increasing $\eta_{ETU}$. The increased importance of upconversion in depletion of the intermediate-level population

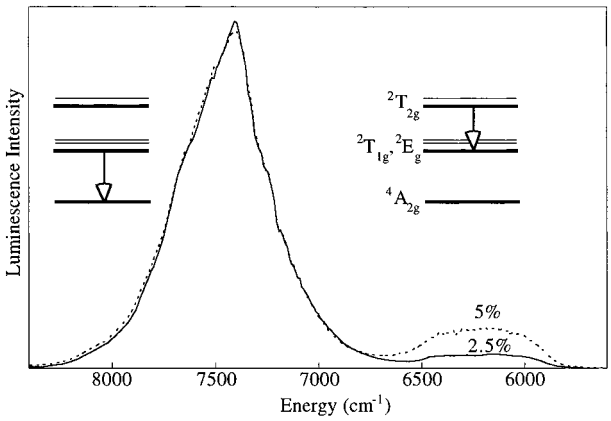


**Figure 7.** Near-IR luminescence (300 K) with 9551 cm$^{-1}$ (1047 nm) near-IR excitation at the highest experimental power shown in Figure 6 (ca. 75 mW/mm$^2$) for 2.5% (—) and 5% (- - -) $Re^{4+}$:$Cs_2ZrCl_6$ dopant concentrations. The emission transition associated with each luminescence feature is indicated schematically. The Si detector response terminates at ca. 5900 cm$^{-1}$.

at higher concentrations is also manifested in the dynamic behavior of this 5% sample, in which shorter intermediate-level lifetimes ($\tau_1(5\%)/\tau_1(2.5\%) \approx 0.62$) and more rapid decay of the upconversion transient curves are observed, while the upper excited-state retains a lifetime ($\tau_2(5\%)/\tau_2(2.5\%) \approx 0.96$) (data not shown) similar to that in the 2.5% sample. Since no cross relaxation pathways are available for concentration quenching of either metastable excited state, the upconversion efficiency of more concentrated samples is expected to be limited only by possible impurity trapping effects.

**iii. Upconversion Temperature Dependence.** Integrated upconversion excitation intensities from the spectra in Figure 5 and additional data at other temperatures are plotted as a function of temperature in Figure 3c. These data reflect the total upconversion luminescence intensity observed under broadband excitation conditions. Although the overall decrease in intensity between low and high temperatures is similar to that of the excited-state lifetimes shown in Figure 3b, the shape of the temperature dependence is unusual in that it shows its most substantial change between 10 and 50 K, where no temperature dependence is observed in the data of Figure 3a,b. To understand the origin of this behavior, the predicted upconversion temperature dependence is calculated by inclusion of temperature in the CW low-power relationship for $N_2$ (eq 6b). The terms $w_{ETU}$, $k_1$, $k_{2a} + k_{2b}$, and $(FN_0)^2$ in eq 6b may each vary with temperature. The temperature dependence of $(FN_0)^2$ is obtained by integration of the squared absorption spectra in the $^2T_{1g}/{}^2E_g$ energy region at a series of temperatures. Note that these integrated *squared* absorption intensities behave differently from the integrated *linear* absorption intensities shown in Figure 3a since they are sensitive to temperature-dependent changes in bandshape. The $^2T_{1g}/{}^2E_g$ absorption features are all observed to broaden between 10 and 50 K despite having constant integrated areas. This broadening, and the resultant change in $(FN_0)^2$, is responsible for the rapid decrease in integrated upconversion intensities observed upon warming from 10 to 50 K. Note that the upconversion intensity temperature dependence observed with monochromatic excitation will not necessarily show this same behavior, but will increase or decrease with temperature depending on the change in absorption cross section at the specific excitation energy. Figure 3b provides the temperature dependencies of $\tau_1$ and $\tau_2$, from which the functions $k_1(T)$ and $(k_{2a} + k_{2b})(T)$ are directly obtained. Thus, three of the four temperature-dependent terms in eq 6b are determined experi-

(35) Modeling the difference between the observed and calculated downconversion data in Figure 6 as deriving from an entirely disjointed $Re^{4+}$ population (rather than a range as described above) allows a value of ca. 45 ± 10% to be estimated for the population of excited ions that show a strictly linear downconversion power dependence.

mentally from absorption and downconversion luminescence data. This allows for determination of the final temperature dependent function $w_{ETU}(T)$ by comparison with the upconversion data of Figure 3c. Two calculated $N_2$ curves based on eq 6b are presented in Figure 3c. The first predicted curve (- - -), assumes no temperature dependence of $w_{ETU}$ (i.e., $w_{ETU}(300\ K) = w_{ETU}(10\ K)$). This calculation reproduces the correct overall behavior of the experimental temperature dependence, but underestimates the high-temperature intensity by a factor of ca. 3 relative to the low-temperature intensity. From this observation, we conclude that $w_{ETU}$ must increase by a factor of approximately 3 in this temperature range. The second predicted curve (----) includes a hyperbolic cotangent function for $w_{ETU}(T)$ similar to those used to fit the absorption data of Figure 3a. Although the exact functional form chosen is arbitrary, inclusion of a $w_{ETU}$ temperature dependence such that $w_{ETU}(300\ K) \approx 3(w_{ETU}(10\ K))$ significantly improves agreement between the calculated and experimental temperature dependence over the entire temperature range.

The experimentally-determined temperature dependence of $w_{ETU}$ concluded above can be compared to that estimated using eq 8, which describes the rate parameter for the energy-transfer

$$w_{ETU,res} = (\text{constant}/\nu^2 n^4 R^6) f_D f_A \int g_D(\nu)\, g_A(\nu)\, d\nu \quad (8)$$

step in terms of the pairwise resonant dipole−dipole donor−acceptor (DA) interactions expected to dominate this process.[36] $R$ is the DA interionic separation, $\nu$ ($cm^{-1}$) is the average energy of the transition, $n$ is the index of refraction at this energy, and $f_D$, $f_A$, $g_D(\nu)$, and $g_A(\nu)$ are the oscillator strengths and spectral bandshape functions for the relevant electronic transitions, respectively. The resonant spectral overlap integrals at 10 and 300 K are determined by integrating the overlap between the normalized $\Gamma_8(^2T_{1g}) \rightarrow \Gamma_8(^4A_{2g})$ luminescence and the estimated $\Gamma_8(^2T_{1g}) \rightarrow \Gamma_8(^2T_{2g})$ ESA spectra (Figure 5) scaled by their oscillator strengths at that temperature. The prefactor does not change appreciably with temperature and therefore cancels when a ratio is taken. This approach yields a ratio of $w_{ETU}(300\ K)/w_{ETU}(10\ K) \approx 72$, which is an order of magnitude larger than the value of 3 determined experimentally from the data in Figure 3c. This discrepancy reflects contributions to the upconversion intensity from additional mechanisms beyond the resonant dipole−dipole mechanism described by eq 8. For example, additional low-temperature overlap between the $\Gamma_8(^2T_{1g}) \rightarrow \Gamma_8(^4A_{2g})$ luminescence and $\Gamma_8(^2T_{1g}) \rightarrow \Gamma_7(^2T_{2g})$ ESA profiles could be attained with loss of only one or more quanta of $\nu_{max} = 342$ $cm^{-1}$ in a phonon-assisted ETU process. While the general form of eq 8 is also applicable to phonon-assisted ETU, the inclusion of phonon-coupled transitions effectively broadens the donor and acceptor spectral functions, and this leads to a smaller temperature dependence than that of the purely resonant overlap described by eq 8. An alternative explanation might involve temperature-dependent migratory excitation loss to traps or other macroscopic phenomena that are experimentally difficult to characterize.

**iv. Upconversion Time Dependence.** While the visible and near-IR downconversion transients show single-exponential decay curves at all temperatures (Figure 4a,b), the 9399 $cm^{-1}$ (1064 nm) excited upconversion transient shows an exponential rise followed by an exponetial decay at all temperatures (Figure 4c). This double-exponential dynamic behavior is a well-known signature for ETU,[37] and reflects the ETU process in two ways. First, the distinctly slow rise time indicates that upper-state population does not occur in the duration of the 10 ns excitation pulse. Second, the decay is over an order of magnitude longer than the natural decay of this state, indicating that the upper-state population is fed continuously by a long-lived intermediate population that is also decaying. The upconversion luminescence rise time is therefore correlated with the lifetime of the probed state, while the decay is related to the lifetime of the feeder state. The temperature dependence of the upconversion transient data follows the general trend expected on the basis of these observations: Both the visible and near-IR luminescent processes become more rapid at higher temperatures due to their increased oscillator strengths, and correspondingly shorter rise and decay times in the upconversion luminescence dynamics are observed (Figure 4c). The upconversion time dependence is therefore qualitatively understood in a straightforward way.

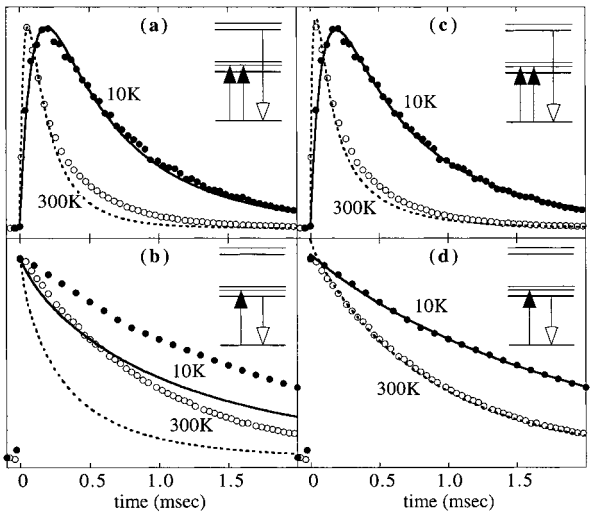


**Figure 8.** Experimental (●, ○) and simulated (— and - - -) 10 and 300 K luminescence dynamics, respectively, for the visible upconversion and near-IR downconversion luminescence transients in 2.5% $Re^{4+}$:$Cs_2ZrCl_6$ measured after a 10 ns (1064 nm) laser pulse. Excitation and luminescence processes for each transient are indicated schematically. Simulated curves were calculated from eq 5 and the parameters in Table 1. Simulated curves in panels a and b were calculated with a single $w_{ETU}$ value (Table 1), and those in panels c and d were calculated using a distribution of $w_{ETU}$ values as described in section III.C.iv.

To extract more information from these transient curves, the luminescence dynamics are quantitatively simulated using the three-level kinetic model depicted in Scheme 2 and described by eq 5, and the experimental kinetic parameters given in Table 1. When short excitation pulses are used, the pulse defines $t = 0$, after which the GSA pump rate constant, $F$, is zero. Only the pump photon density, which combines with the absorption cross section to determine $N_1$ at $t = 0$, is not known experimentally. This parameter was adjusted to optimize simulation of the low-temperature upconversion transient, and then fixed at this value for simulation of the remaining transients. All other parameters required for the simulations of all four transient data sets are defined experimentally (Table 1). These simulations yield excellent reproductions of the upconversion data at both high and low temperatures, as shown in Figure 8a, reproducing the key features of the shortened rise and decay times at elevated temperatures.

(36) Di Bartolo, B. *Optical Interactions in Solids*; Wiley: New York, 1968, Chapter 18. Higher order electric-multipole or magnetic-dipole/multipole contributions are neglected since the dipole−dipole contribution described by eq 8 is expected to dominate.

(37) Buisson, R.; Vial, J. C. *J. Phys. Lett.* **1981**, *42*, L115−L118.

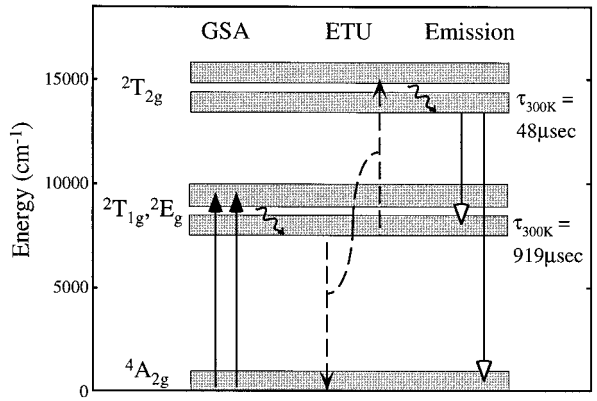


**Figure 9.** Summary of the upconversion mechanism in $Re^{4+}$:$Cs_2ZrCl_6$. The solid lines indicate the radiative processes of GSA and luminescence, and the dashed and wiggled lines indicate the nonradiative processes of ETU and intramanifold multiphonon relaxation, respectively.

Importantly, the near-IR downconversion transients observed under the same conditions are not reproduced by the same parameters that simulate the upconversion curves (Figure 8b). Specifically, the calculated near-IR downconversion curves are distinctly nonexponential, and decay much faster in the short time range than is observed experimentally. This discrepancy is interpreted as reflecting a distribution of upconversion rate constants, $2w_{ETU}N_1$. This conclusion was also reached from analysis of the upconversion and near-IR power dependence data in Figure 6 (*vide supra*). As seen from eq 8, $w_{ETU}$ is heavily dependent upon the interionic separation, R, between donor and acceptor ions in a nonradiative energy-transfer process. Since a statistical distribution of dopant ions in this crystal leads to a range of interionic separations, eq 8 also implies a range of pairwise $w_{ETU}$ values. This was simulated numerically using a shell model approach analogous to that described in detail in ref 38 for rare earth cross relaxation. Like above, the pump photon density in eq 5 was adjusted to optimize simulation of the low-temperature upconversion transient curve, and then fixed at this value for simulation of the remaining transients. As shown in Figure 8c, the introduction of a range in $w_{ETU}$ does not significantly alter the calculated upconversion luminescence transients, since these are dominated by pairs with small *R* values. It does, however, lead to a much improved *simultaneous* reproduction of both the upconversion and near-IR downconversion data, as shown in Figure 8d. To summarize, these data and those in Figure 6 reveal that a sizable portion of the downconversion luminescence observed in these samples derives from ions that are not contributing significantly to the measured upconversion luminescence.[35] This is rationalized by recognizing that whereas downconversion luminescence equally probes all excited ions, upconversion is biased toward detection of ion pairs with small interionic separations, *R*. These observations thus emphasize the distinction between the multiple-center nature of ETU, and the single-center nature of downconversion luminescence.

## IV. Discussion

**A. Key Factors for Upconversion in $Re^{4+}$:$Cs_2ZrCl_6$ and Possible Applications.** Figure 9 summarizes the $Re^{4+}$ upconversion mechanism determined in this study. This process begins with the GSA excitation of two $Re^{4+}$ ions into the $^2T_{1g}/^2E_g$ excited-state manifold by a low-energy light source. These two excited ions then combine in an ETU step in which one ion is promoted to a vibronically-excited level of the $\Gamma_7(^2T_{2g})$ upper excited state, while the second relaxes to the ground state. The doubly-excited ion relaxes nonradiatively within the upper state, and red $\Gamma_7(^2T_{2g}) \rightarrow \Gamma_8(^4A_{2g})$ upconversion luminescence and various near-IR $^2T_{2g} \rightarrow {}^2T_{1g}/^2E_g$ inter-excited-state luminescence transitions are observed. This mechanism is extremely efficient, and under moderate steady-state pumping conditions at reasonably low concentrations the main mechanism for depletion of the intermediate-level population is seen to be upconversion, not downconversion ($2w_{ETU}N_1 \approx 4.2k_1$). Despite an extremely favorable spectral overlap, no evidence for ESA is observed. Since the oscillator strengths of some of these ESA transitions must be fairly large on the basis of the observed radiative transition rates (Table 1) and the excellent GSA/ESA energy match (Figure 5), the absence of ESA features in the upconversion excitation scans of Figure 5 reflects the efficiency of the ETU process rather than the inefficiency of the ESA processes.

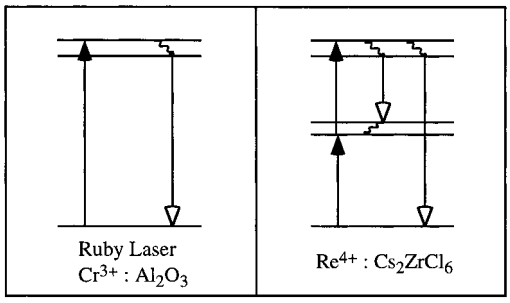


**Figure 10.** Two potential $Re^{4+}$ upconversion laser schemes proposed on the basis of the spectroscopic results in this paper, and compared to the well-known downconversion ruby laser mechanism.

The remarkable efficiency and high-temperature performance of $Re^{4+}$ as a luminescence upconversion ion is attributable to a few key aspects of its electronic structure: (a) The large reduced energy gaps and small excited-state nuclear distortions lead to long lifetimes for two excited states. The long lifetime of the intermediate state is particularly consequential, as it leads to a buildup of the intermediate-level population density and allows other dynamic processes beyond luminescence to occur on a competitive time scale, specifically energy-transfer upconversion. (b) The energetic conditions present for such a two-photon process are ideal, with the $^2T_{2g}$ manifold of states being almost exactly twice the energy of the lowest-energy $^2T_{1g}/^2E_g$ excited-state sublevel, $\Gamma_8(^2T_{1g})$. (c) The spin selection rules and state multiplicities favor inter-excited-state transitions rather than those involving the ground state. (d) Doubly-excited $Re^{4+}$ ions quickly relax to an upper-excited-state level having no accessible cross relaxation pathway. The large energy gaps and lack of cross relaxation combine to ensure efficient channeling of ETU excitation into luminescent processes rather than nonradiative relaxation processes.

The fast vibronic relaxation observed within the upper manifold is akin to the contribution of the third level in a three-level laser. A close electronic analog to $Re^{4+}$ is the $d^3$ $Cr^{3+}$ center at the heart of the ruby laser. In ruby, $Cr^{3+}$ ions excited by pumping the spin-allowed $^4T_{2g}$ and $^4T_{1g}$ absorption features rapidly relax to the long-lived $^2E_g$ state, from which stimulated emission is attainable. The analogy between the ruby downconversion lasing action and the upconversion luminescence observed in $Re^{4+}$:$Cs_2ZrCl_6$ is illustrated in Figure 10, showing a possible three-level upconversion laser scheme involving $Re^{4+}$. A second potential laser scheme is also indicated in Figure 10,

(38) Vasquez, S. O.; Flint, C. D. *Chem. Phys. Lett.* **1995**, *238*, 378−386.

involving a four-level inter-excited-state lasing process that would be tunable between ca. 4300 and 5400 $cm^{-1}$ (ca. 1.8−2.3 $\mu$m) on the basis of the vibronic width of these luminescence features. Experiments to pursue the laser potential of this ion in both energy regions are planned.

**B. Relationship between $Re^{4+}$ Electronic Structure and Photoredox Reactivity.** $Re^{4+}$ and its $d^3$ electronic-structure homologs, $Mo^{3+}$ and $W^{3+}$, with octahedral halide (*e.g.*, $ReCl_6^{2-}$), amine (*e.g.*, $(tmtacn)MoCl_3$), and/or thiocyanate (*e.g.*, $Mo(NCS)_6^{3-}$) ligation, have received attention recently as attractive starting materials in photoinitiated multielectron redox reactions.[20−23] This reactivity involves one-electron oxidation of an electronically-excited $d^3$ ion by a suitable electron acceptor species, after which further redox transformations of the transition metal in its oxidized ground state become spontaneous. The key step in accessing this interesting chemistry is the excited-state electron-transfer reaction involving an excited $d^3$ ion. Two related aspects of the electronic structure of these $d^3$ ions can be identified as having a large impact on their ability to perform such reactions: (a) their large energy gaps and (b) their small excited-state nuclear distortions.

In octahedral complexes of all three of these second- and third-row $d^3$ ions, the lowest-lying excited state is always approximately 8000−11000 $cm^{-1}$ (ca. 1−1.4 eV) above the ground state.[39] The resulting reduced energy gaps are large since these energies are 1-2 orders of magnitude larger than their typical M−L vibrational energies. The small excited-state nuclear distortions derive from the nature of the electronic promotions: In all three of these ions, the lowest excited states involve intra-$t_{2g}$ spin-flip transitions, and therefore generate essentially no change in M−L bonding or geometry ($\Delta r_{ex}(\Gamma_8(^2T_{1g})) = +0.01$ Å from Figure 2, for example[40]). The combination of large energy gaps and small nuclear distortions in the lowest-energy excited states ($^2T_{1g}/^2E_g$) of these ions allow them to still luminesce in solutions where additional high-frequency solvent modes may contribute to $k_{decay}$. From the published $\Gamma_8(^2T_{1g})$ 300 K solution lifetime data of $ReCl_6^{2-}$ in $CH_3CN$,[21] $k_{nr}$ is seen to be 8250 times larger than $k_{rad}$ (Table 1), and still the excited-state species has a sufficient lifetime ($\tau_1 = 80$ ns) to be involved in bimolecular redox reactions, for which ca. 10−50 ns is typically required.[41] Thus, the large energy gap and small nuclear distortion provide a sufficient excited-state lifetime to allow the observed photoredox chemistry.

These excited-state distortions are small because no change in M−L bonding accompanies the spin-flip excitations. Similarly, one-electron oxidation of these ions involves removal of a weakly-antibonding $t_{2g}(d_\pi)$ electron, again causing only a small change in bonding and, hence, in geometry.[42] As a result, these transition-metal ions do not make any significant contribution to the Franck−Condon properties of their photoredox transformations, and the nuclear coordinates of their electron-transfer reactions are essentially only those inherent to the acceptor species. The main perturbation upon excitation of these ions is the change in redox potential, which is more negative in the excited state by ca. $E_{0-0}$, as described by the Rehm−Weller equation.[43,44] Electronic excitation in these $d^3$ ions thus contributes an additional ca. 1 eV to driving an electron-transfer reaction, while their small nuclear distortions accompanying excitation and oxidation minimize the nuclear reorganization energy associated with this reaction. According to nonadiabatic electron-transfer theory,[45,46] small nuclear reorganization energies allow electron--transfer reactions to proceed at lower driving forces, $\Delta G°$. These properties may therefore facilitate excited-state electron-transfer reactivity at near-zero (or positive) $\Delta G°$ values, as was recently reported.[20,21]

In summary, the large energy gaps and small excited-state nuclear distortions of $ReCl_6^{2-}$ lead to the long lifetimes, purely radiative decay rates, and upper excited-state emission in the solid state, making upconversion luminescence both possible and efficient. These two properties also lead to substantial solution $^2T_{1g}/^2E_g$ excited-state lifetimes in this and related $d^3$ ions, a requirement for bimolecular excited-state reactivity. The minimal nuclear reorganization that occurs upon oxidation of these ions, attributable to the weak antibonding character of the redox-active orbital, additionally contributes to the photoredox reactivity of these ions by allowing electron-transfer reactions with smaller driving forces to be kinetically accessible. The same electronic structure characteristics of these second- and third-row $d^3$ ions that make them attractive photophysically are therefore also responsible for their attractive photochemistry.

## V. Conclusion

The two-photon luminescence upconversion observed in $Re^{4+}:Cs_2ZrCl_6$ represents the first time such a phenomenon has been observed in a $d^3$ transition-metal ion.[11] This system significantly expands the relatively short list of known transition-metal upconversion promoters,[6−11] both in number and in accessibility of the phenomenon to potential ambient-temperature materials applications. The extremely efficient $Re^{4+}$ upconversion is largely attributable to inherent electronic-structural properties of the $Re^{4+}$ ion itself, including its large energy gaps and undisplaced excited-state potential surfaces. These same properties are influential in the photoredox chemistry of this and related ions. Since the relevant electronic states are ligand-field independent, $Re^{4+}$ upconversion is expected to be generally adaptable to a wide variety of hosts and coordination environments. This is an important consideration in view of possible functional application of this phenomenon in photonics materials. Directly accessible applications include the use of this ion as a red luminophore in upconversion-based imaging or quantum-counting materials, or as an active ion for generating red or near-IR laser emission based on upconversion excitation. Further studies are underway to explore the photophysics of this system, as well as those of other related transition-metal ions.

**Acknowledgment.** We thank M. Pollnau and M. Wermuth for many valuable discussions. This research has been supported by the Swiss National Science Foundation.

## Appendix: Experimental Determination of $w_{ETU}$

Near-IR luminescence decay data at short times after a pulse can be used to determine the magnitude of $w_{ETU}$.[32] At short

(39) Lever, A. B. P. *Inorganic Electronic Spectroscopy*, 2nd ed.; Elsevier: Amsterdam, 1984.
(40) Determined from $S(a_{1g}) = 0.20$, $\nu_1 = 342$ $cm^{-1}$, $\mu = 35.45$ g/mol, and the modal description $Q$ (Å) $= \sqrt{6}r$ (Å).
(41) Winkler, J. R.; Gray, H. B. *Inorg. Chem.* **1985**, *24*, 346−355.
(42) Although no structural data for $ReCl_6^-$ are available, IR vibrational data show only very small shifts (ca. ±10 $cm^{-1}$) upon oxidation, thus reflecting only small changes in bonding. See for example: Frais, P. W.; Lock, C. J. L.; Guest, A. *J. Chem. Soc., Chem. Commun.* **1970**, 1612−1613.
(43) Rhem, D.; Weller, A. *Isr. J. Chem.* **1970**, *8*, 259−271.
(44) Jones, W. E., Jr.; Fox, M. A. *J. Phys. Chem.* **1994**, *98*, 5095−5099.
(45) Marcus, R. A.; Sutin, N. *Biochim. Biophys. Acta* **1985**, *811*, 265−322.
(46) Brunschwig, B. S.; Sutin, N. *Comments Inorg. Chem.* **1987**, *6*, 209−235.

times after the pulse, eq 5 yields

$$dN_0/dt = k_1N_1 + w_{ETU}(N_1)^2$$
$$dN_1/dt = -k_1N_1 - 2w_{ETU}(N_1)^2 \quad \text{(A1)}$$
$$dN_2/dt = w_{ETU}(N_1)^2$$

Denoting $N_1(t = 0) = N_1(0)$, integration yields

$$N_1(t) = N_1(0)\exp(-t/\tau_1)/\{1 + 2w_{ETU}N_1(0)[\tau_1(1 - \exp(-t/\tau_1))]\} \quad \text{(A2)}$$

Rearranging yields an expression having linear form with a slope proportional to $w_{ETU}$:

$$(N_1(0)/N_1(t))\exp(-t/\tau_1) - 1 = 2w_{ETU}N_1(0)[\tau_1(1 - \exp(-t/\tau_1))] \quad \text{(A3)}$$

Plotting the near-IR decay curve as $(N_1(0)/N_1(t))\exp(-t/\tau_1) - 1$ vs $[\tau_1(1 - \exp(-t/\tau_1))]$ therefore leads to a linear slope of $2w_{ETU}N_1(0)$ at short times after the pulse.

Data were collected at three powers for 2.5% Re:$Cs_2ZrCl_6$. Homogeneous photon densities were generated by passing an unfocused 10 ns 9399 $cm^{-1}$ (1064 nm) pulse from a Nd:YAG laser through a 110 micrometer diameter pinhole immediately in front of the sample to generate a homogeneous collimated excitation beam. Measured powers were converted to photon densities, and a polished sample with known optical density and length was used, allowing the initial excitation density, $N_1(0)$, to be determined at each excitation power. The transformed data are shown in Figure 11, along with the linear least-squares best fit to the early time data for each experimental curve. From these fits, an average value of $w_{ETU} = 5.8 \times 10^{-16}$ $cm^3/s$ is determined, with error bars estimated to be ca. 50% on the basis of the range of measured values and estimated errors in absorbed powers.

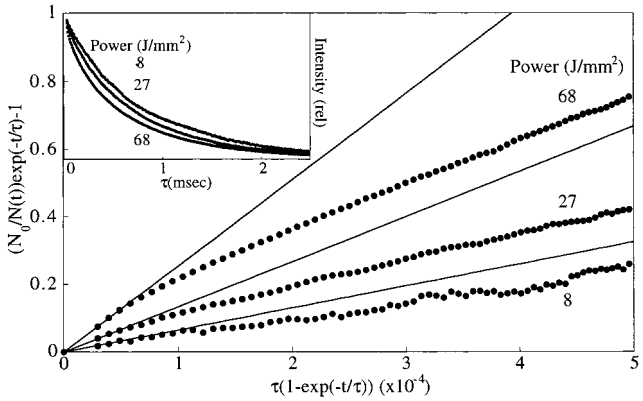


**Figure 11.** Near-IR downconversion luminescence decay data (300 K) for 2.5% $Re^{4+}$:$Cs_2ZrCl_6$ at different excitation powers, plotted as described in the Appendix. Linear fits to the short-time region provide numerical estimates of $2w_{ETU}N_1(0)$, from which an average $w_{ETU}$(300 K) = $5.8 \times 10^{-16}$ $cm^3$ $s^{-1}$ (±50%) is determined. Inset: Untransformed near-IR decay data showing the variation in lifetime with excitation power.

IC990556R